Physics of Fluids

RESEARCH ARTICLE | AUGUST 01 2024

Dynamics of bubble formation on superhydrophobic surface under a constant gas flow rate at quasi-static regime

Daniel O'Coin ; Hangjian Ling

Physics of Fluids 36, 083303 (2024)
https://doi.org/10.1063/5.0219321

AIP Publishing

Dynamics of bubble formation on superhydrophobic surface under a constant gas flow rate at quasi-static regime

Cite as: Phys. Fluids **36**, 083303 (2024); doi: 10.1063/5.0219321
Submitted: 16 May 2024 · Accepted: 15 July 2024 ·
Published Online: 1 August 2024

Daniel O'Coin and Hangjian Ling[a)]

AFFILIATIONS

Department of Mechanical Engineering, University of Massachusetts Dartmouth, Dartmouth, Massachusetts 02747, USA

[a)]Author to whom correspondence should be addressed: hling1@umassd.edu

ABSTRACT

In this work, we experimentally studied bubble formation on the superhydrophobic surface (SHS) under a constant gas flow rate and at quasi-static regime. SHS with a radius R_{SHS} ranging from 4.2 to 19.0 mm was used. We observed two bubbling modes A and B, depending on R_{SHS}. In mode A for small R_{SHS}, contact line fixed at the rim of SHS, and contact angle (θ) initially reduced, then maintained as a constant, and finally increased. In mode B for large R_{SHS}, contact line continuously expanded, and θ slowly reduced. For both modes, during necking, contact line retracts, and θ was close to the equilibrium contact angle. Moreover, the pinch-off of bubble at the early stage was similar to the pinch-off of bubble from a nozzle and followed a power-law relation $R_{neck} \sim \tau^{0.54}$, where R_{neck} is the minimum neck radius and τ is the time to detaching. Furthermore, we calculated the forces acting on the bubble and found a balance between one lifting force (pressure force) and two retaining forces (surface tension force and buoyancy force). Last, we found a waiting time for a finite volume to be detected for large R_{SHS}. The detached volume was well predicted by Tate volume, which was derived based on balance between buoyancy and surface tension and was a function of bubble base radius.

I. INTRODUCTION

The formation of a gas bubble on a solid surface submerged under liquid, either through an orifice or a nozzle, has been an active area of multiphase flows research for decades. Understanding the bubble formation is crucial for many industrial and biomedical applications, for example, pool boiling heat transfer,[1–5] froth floatation,[6] surface cleaning,[7,8] and drug deliver.[9–11] Predicting and controlling the bubble size are highly demanded in these applications since the bubble size determines the heat and mass transport. Recently, micro-/nano-textured superhydrophobic surface (SHS) has also received growing attention due to its unique properties, including drag reduction,[12–14] anti-icing,[15,16] anti-biofouling,[17,18] and anti-corrosion.[19,20] The SHS is best known for its large equilibrium contact angle ($\theta_0 > 150°$) and the ability to entrap gas between surface textures when contacted with water[21] (i.e., the formation of Cassie–Baxter state[22]). Despite the wide applications of both SHS and bubble formation, however, there are very limited studies of bubble formation on SHS.[23–26] The textured SHS was shown to promote the formation of larger bubbles than the smooth hydrophobic and hydrophilic surfaces[23] and thereby might involve different dynamics that control the bubble growth. This study aims to better understand the dynamics of bubble formation on SHS under a constant gas flow rate at the quasi-static region.

First, we briefly review past studies on bubble formation on hydrophobic and hydrophilic surfaces, through an orifice or a nozzle. A comprehensive review of this topic can be found in several review articles.[27–30] The bubble formation and bubble detached volume V_d were found to be affected by many factors, including the material properties of the liquid,[31,32] liquid height,[33] nanoparticle suspension,[34,35] compound interface,[36] reduced gravity,[37,38] gas flow condition,[39] and size and shape of the orifice.[40–42] Among them, the effect of gas flow rate Q received the most attention.[43] With increasing Q, the bubble formation experienced two regimes: quasi-static regime and dynamic regime. At the quasi-static regime with low Q, many studies[40,44] showed that V_d was independent of Q and can be well predicted by Tate volume,[45] which was derived based on balance between buoyancy and surface tension forces. The equilibrium bubble shape was theoretically predicted by solving the Young–Laplace equation with given boundary conditions.[46–48] At the dynamic region with large Q, V_d increased with Q and followed power-law relations: $V_d \sim Q^{6/5}$ for inviscid liquid[49,50] and $V_d \sim Q^{3/4}$ for highly viscous liquid.[51,52] As

continuously increasing Q, the bubble formation transitioned from period-1 to period-2 and chaotic bubbling regimes, where successive bubbles coalesced with each other before detachment.[53,54]

The effect of surface wetting condition on the bubble formation was also extensively investigated.[55–63] The wettability of a surface was characterized by θ_0 with good wetting (hydrophilic) and poor wetting (hydrophobic) surfaces having $\theta_0 < 90°$ and $\theta_0 > 90°$, respectively. A large $\theta_0 \sim 110°$ was obtained by using paraffin or Teflon coated surfaces,[59,61] and a small $\theta_0 < 30°$ was achieved by reducing the surface tension of water.[58,62] Depending on θ_0, the bubble formation followed two different modes A and B, two terms first introduced by Chester[63] and later used by several other researchers.[23,59] The two modes were distinct due to the different behaviors of contact line during the growth of the bubble: in mode A the contact line pinned at the orifice rim, while in mode B, the contact line spread beyond the orifice and moved along the horizontal surface. It was also found that the maximum bubble base radius and V_d were independent of θ_0 in mode A, but increased as increasing θ_0 in mode B.[59] Mode A was mostly observed on hydrophilic surfaces, and mode B was primarily seen on hydrophobic surfaces. Due to a larger base radius, hydrophobic surfaces usually had a larger V_d than hydrophilic surfaces.[56,58,60] Bubble formation involving a moving contact line was numerically predicted by a stick-slip model.[55,62] Furthermore, it was found that the relationships between V_d and Q for surfaces with different θ_0 followed a same curve after proper normalizations.[61,62]

The bubble formation on the superhydrophobic surface with $\theta_0 > 150°$ received far less attention.[23–26] Gerlach *et al.*[59] numerically varied θ_0 from 40° to 170° and found an increase in bubble base radius and thereby an increase in V_d as increasing θ_0. Rubio-Rubio *et al.*[23] and Qiao *et al.*[24] experimentally studied the bubble formation on a SHS with $\theta_0 = 165°$ and 156°, respectively, at the quasi-static regime. Both found that with increasing the radius of SHS (R_{SHS}), the bubble formation transitioned from mode A (pinning contact line) to mode B (moving contact line), and V_d increased as increasing R_{SHS} during mode A. The critical SHS radius (R_{cr}) for the transition (i.e., the maximum bubble base radius in mode B), according to Rubio-Rubio *et al.*, was a function of θ_0. For $\theta_0 = 165°$, $R_{cr} = 8.7$ mm.[23] Furthermore, Rubio-Rubio *et al.* showed that the bubble shape can be predicted by solving the Young–Laplace equation. Breveleri *et al.*[26] measured the bubble formation on a SHS fabricated on a porous material and found a larger bubble size as increasing the pressure of the gas injection.

The goal of this study is to better understand the bubble formation on SHS under a constant gas flow rate at the quasi-static regime. Different from prior works by Rubio-Rubio *et al.*[23] and Qiao *et al.*,[24] we will perform a force balance analysis to understand the dominant forces acting on the bubble. We will pay more attention to the bubble necking process, including the variations of minimum neck radius and contact angle. Moreover, given the success of Tate volume to predict V_d for hydrophilic and hydrophobic surfaces at the quasi-static regime,[61,62] we will test whether the Tate volume can also be used to predict V_d for SHS. In the following, we describe the experimental methods in Sec. II, results and discussion in Sec. III, and conclusions in Sec. IV.

II. EXPERIMENTAL METHODS

A. Experimental setup

The experimental setup for studying the bubble formation on a SHS is shown in Fig. 1. A transparent tank made of acrylic is filled with water. The tank has an inner dimension of 100 × 100 mm^2. The height of the water is maintained at 70 mm. These dimensions ensure that the walls and the upper free surface have a negligible impact on the bubble formation. At the bottom of the tank, a 50 × 50 mm^2 aluminum surface is installed. The center area with a radius of R_{SHS} of this aluminum surface is made to be superhydrophobic. Outside this region, the surface is hydrophilic. The equilibrium water contact angles (θ_0) on the superhydrophobic and hydrophilic regions measured by placing a small water drop on the surface are 152° ± 2° and 32° ± 2°, respectively. The sliding angle of a water droplet on the SHS is 5° ± 2°. The procedure of creating the SHS is similar to these utilized in our

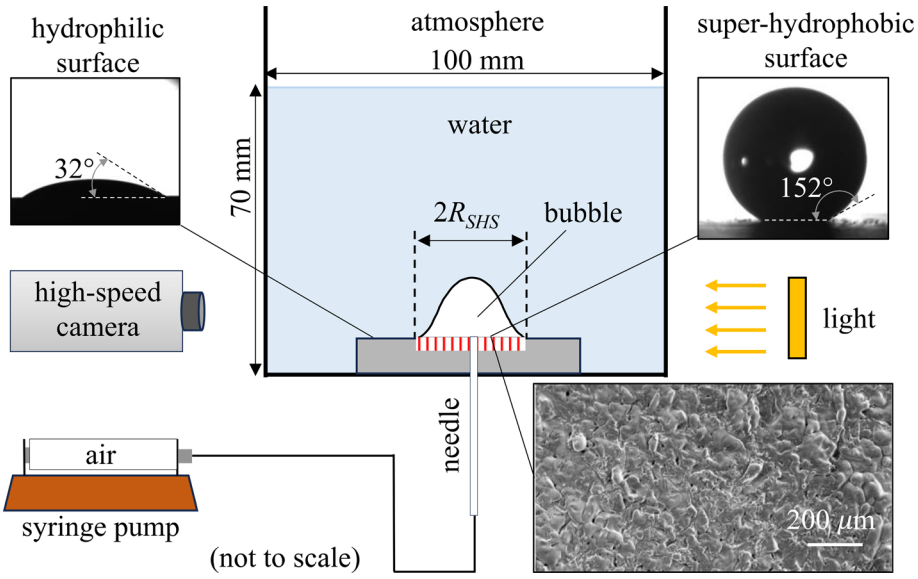

FIG. 1. Experimental setup for studying bubble formation on a superhydrophobic surface with radius R_{SHS}.

early work[18,64] and is briefly described below. First, surface roughness is fabricated on the entire aluminum surface by sandblasting (abrasive medium aluminum oxide, grit size 60, and particle mesh size 35–100). The surface is clean in the ultrasonic bath before and after applying the sandblasting. Then, superhydrophobicity is achieved by spray-coating the rough surface with hydrophobic nano-particles (*Glaco Mirror Coat Zero*, by *SOFT99 Corp*). Only the center aera with the radius of R_{SHS} is coated. A scanning electron microscopy image of the surface texture of the SHS created by the above procedure is also shown in Fig. 1.

A 0.5 mm diameter orifice is fabricated at the center of the SHS to allow the gas to be injected into the bubble. The gas flow is generated and controlled by a syringe pump (Model #NE-1010 SyringeONE, by New Era Pump System Inc). Similar to the setup used by Mirsandi *et al.*,[62] a long needle with a length of 152 mm and an inner diameter of 0.61 mm is used to guide the gas to the orifice. As explained by Mirsandi *et al.*, the purpose of this long needle is to achieve a large pressure drop so that the pressure variation in the bubble does not cause a notable change of the pressure in the syringe. As will be shown later, during the bubble growing process, a constant gas flow rate is achieved in current study.

A high-speed camera (PCO.dimax S4, pixel size 11 μm, 2016 × 2016 pixels) is used to record the bubble formation and detachment. A collimated light (Thorlabs, model #QTH10, power 50 mW) with a diffuser is used to illuminate the bubble. To record the bubble growing process, a frame rate of from 50 frames per second (fps) is used. To record the necking process which occurs at a very short timescale, a frame rate of 1000 fps is used. The spatial resolution of the imaging system is 34 μm/pixel. The data are recorded after a series of bubbles have formed and detached from the surface. The light is turned on for a short duration of time and has negligible influence on the temperature of the water.

The key experimental parameters are listed in Table I. Three values of $R_{SHS} = 4.2$, 6.3, and 19.0 mm are used in the current study. The reason for choosing these values is to cover the two modes A and B of bubble formation as previously reported.[23,63] As shown in Figs. 2(a)–2(c), the two modes are observed in the current study (Multimedia view). In mode A for small $R_{SHS} = 4.2$ and 6.3 mm, as bubble grows, the contact line quickly pins at the rim of the SHS after an initial expansion. As a result, the bubble base radius R_b reaches a maximum value of $R_b^{\max} = R_{SHS}$. In mode B for large $R_{SHS} = 19.0$ mm, the contact line expands and never reaches the edge of SHS. The maximum bubble base radius is $R_b^{\max} = 7.5$ mm, which has a fair agreement with the numerical simulations by Ref. 59 and the experimental observation in Ref. 23. The values of $R_b^{\max}$ for the three cases are provided in Table I. As will be shown later, the two cases for mode A ($R_{SHS} = 4.2$ and 6.3 mm) are sufficient to understand the bubble formation in mode A since the bubble geometrical parameters and the forces acting on the bubble follow similar trends regardless of R_{SHS}. Moreover, the one case for mode B ($R_{SHS} = 19.0$ mm) is sufficient, since in mode B, the bubble has the same maximum based radius ($R_b^{\max} = 7.5$ mm) and same geometrical parameters regardless of R_{SHS}. Readers can find more detailed discussions of the impact of R_{SHS} on the bubble detached volume and bubble formation mode in the works by Rubio-Rubio *et al.*[23] and Qiao *et al.*[24]

TABLE I. Summary of experimental parameters in the current study.

Mode	R_{SHS} (mm)	$R_b^{\max}$ (mm)	$R_b^{\max}/l_\sigma$	Q (ml/min)	Q/Q_{cr}
A	4.2	4.2	1.5	1.2	0.0023
A	6.3	6.3	2.3	1.2	0.0016
B	19.0	7.5	2.8	1.2	0.0014

Also listed in Table I is the gas flow rate $Q = 1.2$ ml/min for all three cases. The value of Q is calculated by fitting the curve of bubble volumes at the constant flow region. The bubbling frequency is less than 0.2 Hz, minimizing the impact of previously formed bubble on the reference one. Moreover, the small value of Q ensures a quasi-static condition. According to Rubio-Rubio *et al.*,[23] the critical flow rate for a transition to dynamic region can be estimated as $Q_{cr} = \pi(16/3g^2)^{1/6}(\sigma R_b^{\max}/\rho_L)^{5/6}$, where $\sigma = 72$ mN/m is the surface tension of water, $\rho_L = 997$ kg/m^3 is the density of water, and $g = 9.78$ m^2/s is the gravitational acceleration. As shown in Table I, Q/Q_{cr} is much smaller than 1. Table I also lists the dimensionless $R_b^{\max^*} = R_b^{\max}/l_\sigma = (Bo)^{1/2}$, where $l_\sigma = (\sigma/\rho_L g)^{0.5} = 2.7$ mm is the capillary length and Bo is the Boud number.

B. Data analysis and force calculation

To characterize the shape of the bubble as it grows, we calculate several parameters, including the volume (V), base radius (R_b), height (H), radius at the apex (R_a), and contact angle at the three-phase contact line (θ). The definitions of R_b, H, R_a, and θ are shown in Fig. 3(a). These geometrical parameters are obtained by processing a binarized image as shown in Fig. 3(c). This binarized image is obtained setting an intensity threshold to the image shown in Fig. 3(b), which is calculated by subtracting an image containing only the wall from the raw image. Then, V is calculated by accumulating the cross section area at each height level from the bottom to the top of the bubble. R_a is obtained by fitting the bubble apex with a circle of radius R_a. θ is found by linearly fitting the bubble shape near the three-phase contact line. The velocity of bubble in the vertical direction is also estimated as $U_b = \mathrm{d}H/\mathrm{d}t$,[47] where t is the time.

To understand the forces acting on the bubble, we follow Mohseni *et al.*[39,65] and calculate six forces, as summarized in Table II. The six forces include two lifting forces (pressure force F_P and gas momentum force F_{GM}) and four restraining forces (surface tension force F_S, buoyancy force F_B, drag force F_D, and liquid inertia force F_{LI}). The pressure force is mainly caused by the surface tension at the bubble apex, which leads to a higher pressure in the bubble than that in the liquid ($2\sigma/R_a$ is the Laplace pressure at the bubble apex). The gas momentum force is due to the momentum of the gas flowing through the orifice. The surface tension force applies at the three-phase contact line of the bubble base. The buoyancy force is due to the hydrostatic pressure applied on the bubble surface. As will be shown later, F_B for bubble presented on SHS is mostly in the downward direction, which is in opposite to bubble formation at a nozzle. The liquid inertia force accounts for the momentum of surrounding liquid due to the acceleration of the bubble as it grows. The drag force is approximated as the force applied on a bubble of radius R_b moving at a constant velocity U_b in the liquid. The drag coefficient C_D takes the form of $C_D = 24/Re_b(1 + 0.15Re_b^{0.687})$,[66] where $Re_b = \rho_L U_b R_b/\mu_L$ is the Reynolds number and $\mu_L = 1.0 \times 10^{-3}$ N s/m^2 is the dynamic viscosity of the water. This expression is valid for the current range of $Re_b < 1000$.

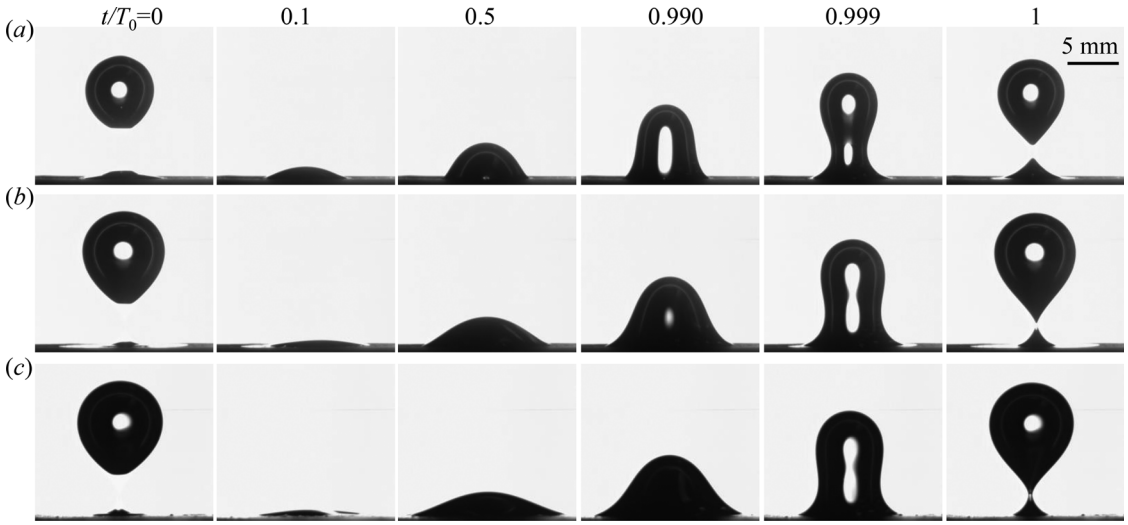

FIG. 2. (a)–(c) Evolutions of bubble shape on SHS with $R_{SHS} = 4.2$ mm (a), 6.3 mm (b), and 19.0 mm (c). For $R_{SHS} = 4.2$ and 6.3 mm, the contact line quickly pins at the rim of SHS (mode A). For $R_{SHS} = 19.0$ mm, the contact line moves but never reaches to the edge of SHS (mode B). $t = 0$ is defined as the time of the detachment of previous bubble, T_0 is the bubbling period, and necking occurs at $t \sim 0.99T_0$. Multimedia available online

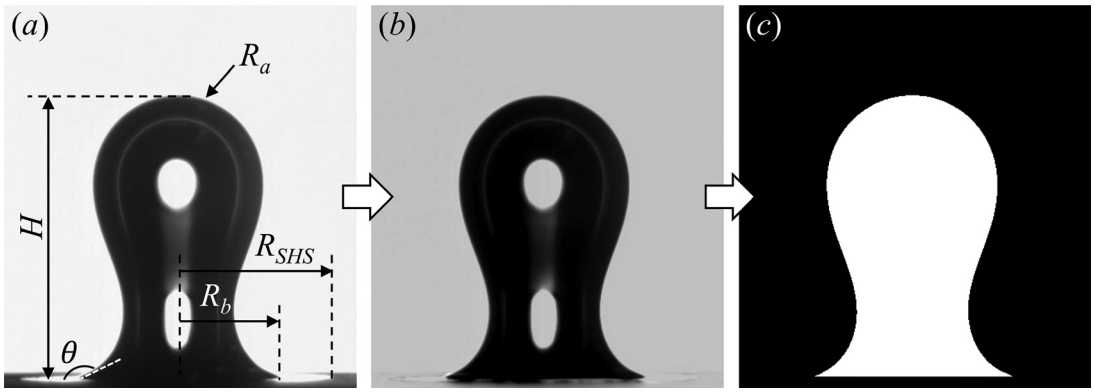

FIG. 3. Definitions of bubble geometrical parameters and image process procedure: (a) a raw image; (b) image obtained by subtracting the wall from the raw image; and (c) binarized image.

TABLE II. Expressions and directions of six forces acting on the bubble as it grows on SHS. Here, $\rho_G = 1.3$ kg/m^3 is the density of air, and negative sign indicates the force is the downward direction.

Forces	Expressions	Direction
Laplace pressure force	$F_P = (2\sigma/R_a + \rho_G g H)\pi {R_b}^2$	Upward
Gas momentum force	$F_{GM} = \rho_G Q^2/\pi {R_b}^2$	Upward
Surface tension force	$F_S = -2\pi R_b \sigma \sin\theta$	Downward
Buoyancy force	$F_B = (\rho_L - \rho_G)gV - \rho_L g H \pi {R_b}^2$	Downward
Liquid inertia force	$F_{LI} = -(11/16\rho_L + \rho_G)\,[V\,dU_b/dt + U_b\,dV/dt]$	Downward
Viscous drag force	$F_D = -1/2\ \rho_L C_D\ \pi {R_b}^2 {U_b}^2$	Downward

The uncertainties of measurement parameters are mainly caused by the errors in determining the boundary of the bubble during the image processing. To estimate the measurement uncertainties, we select different intensity thresholds to get binarized images of the bubble and bubble boundaries. We found that the uncertainty of H is about the size of a pixel (34 μm), the uncertainty of R_b is 0.1 mm, the uncertainty of R_a reduces as increasing bubble volume and varies in the range of 0.5–0.05 mm, the uncertainty of V is 0.004 ml, and the

uncertainty of θ is about 5°. Based on the uncertainties of geometrical parameters, the uncertainties of forces are also calculated and fall below 0.1 mN. When plotting the uncertainties on the figures, they are mostly smaller than the size of the symbols and thereby are not shown.

III. RESULTS AND DISCUSSION

A. Bubble volume

Figure 4(a) shows the evolution of bubble shape during the initial 2 s of the bubbling period, and Fig. 4(b) shows the variations of bubble volume as a function of time (t). For the smallest $R_{SHS} = 4.2$ mm, V increases linearly with t, indicating a constant gas flow rate. Very interestingly, for the two large R_{SHS}, there is a "waiting time" for a bubble with a detected volume to appear. The waiting time is more obvious for larger R_{SHS}, with a magnitude increasing from ~1 to ~2 s as increasing R_{SHS} from 6.3 to 19.0 mm. After the waiting time, a bubble with finite volume is detected and V increases linearly with t. The slope of V for the three cases is nearly the same, indicating nearly the same gas flow rate. The detached volume (V_d) increases as increasing R_{SHS}, in agreement with Rubio-Rubio *et al.*[23] and Qiao *et al.*[24]

Note that the observed waiting time is not due to the measurement uncertainty. Given the uncertainty of bubble volume is 0.004 ml and the flow rate is $Q = 1.2$ ml/min, the uncertainty of the waiting time is 0.2 s. To understand the reason for waiting time for SHS with large R_{SHS} (cases with $R_{SHS} = 6.3$ and 19.0 mm), we show the time variations of F_P (i.e., the primary lifting force acting on the bubble) in Fig. 4(c). Clearly, for the two large R_{SHS}, during the waiting time, F_P is close to 0, which can be explained by the nearly flat bubble interface as shown in Fig. 4(a). During the waiting time, the syringe pump continuously supplies gas, causing the pressure of gas in the orifice to increase. When the gas pressure in the orifice is sufficient to overcome the hydrostatic pressure above the air–water interface, the interface deforms, F_P becomes finite, leading to the subsequent growth of the bubble. As shown in supplementary material, Fig. S1, the waiting time reduces as increasing Q, probably due to the reduced buildup time for the gas to overcome the hydrostatic pressure. Waiting time was also observed for the bubble formation at a micro-orifice[65,67,68] due to a different mechanism. For micro-orifice, the waiting time is because when a micro-size bubble forms at the micro-orifice, the pressure inside the bubble is larger than the pressure in the gas reservoir.[65]

B. Bubble geometrical parameters

Figures 5(a)–5(c) show the variations of H/l_σ, R_b/l_σ, and R_a/l_σ as a function of V/l_σ^3 for the three different R_{SHS}. Figures 5(d)–5(f) show the results as a function of t/T_0 (here, T_0 is the bubbling period). The capillary length l_σ is chosen as the length scale to normalize the geometrical parameters. The evolutions of H, R_b, and R_a for different R_{SHS}

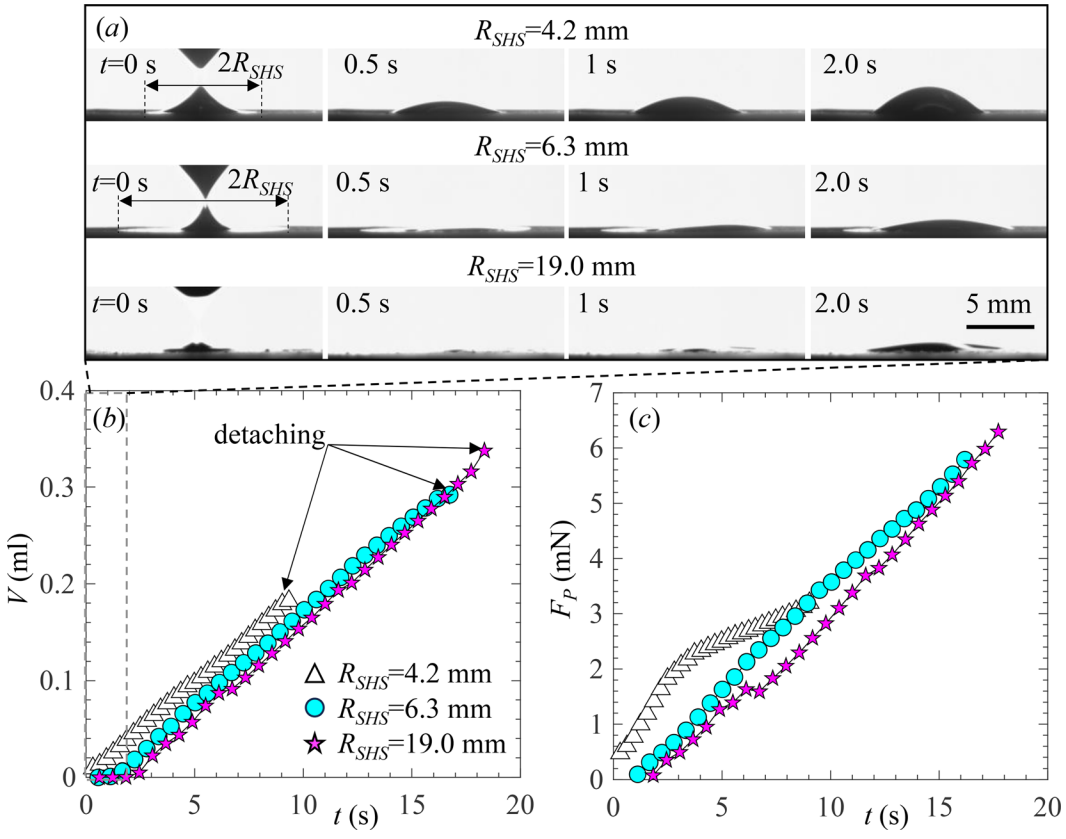

FIG. 4. (a) Evolution of bubble shape at the initial 2 s of the bubbling period on three different SHSs; and (b) and (c) variations of bubble volume (b) and F_P (c) as a function of time (t) for three different SHSs.

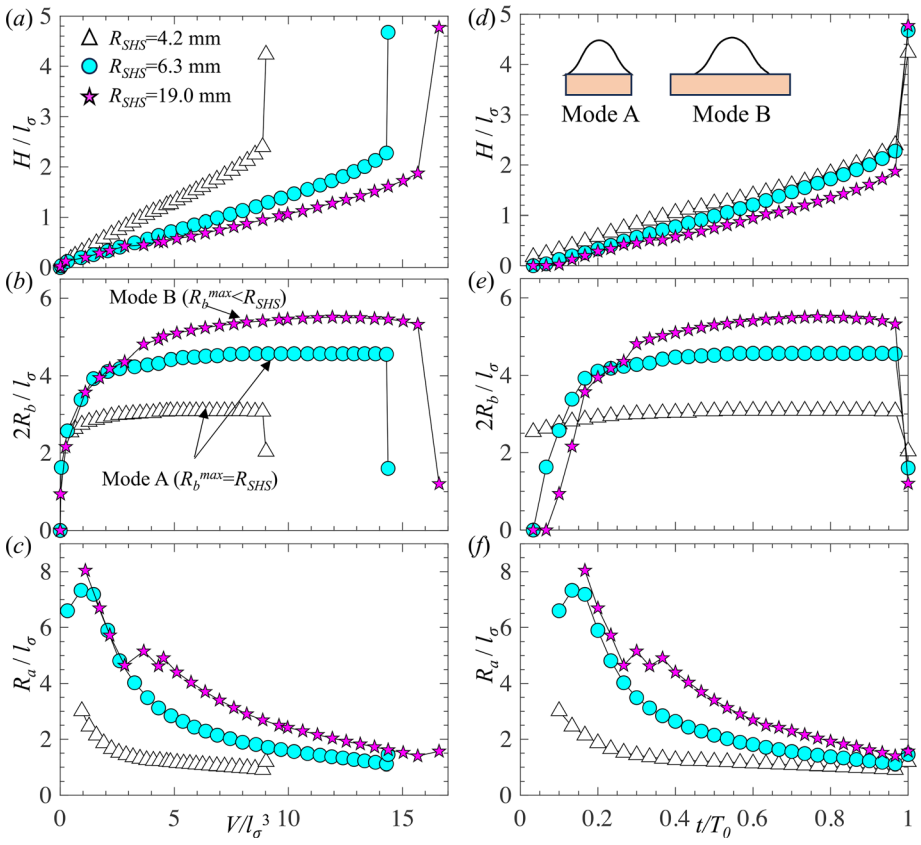

FIG. 5. Variations of H/l_σ, R_b/l_σ and R_a/l_σ as a function of V/l_σ^3 (a)–(c) and as a function of t/T_0 (d)–(f).

generally follow the same trends as described below. H increases linearly with V and t until experiencing a rapid jump due to the necking; R_b experiences an initial increase due to the expansion of contact line, then a nearly constant region, and finally a sudden reduction due to contraction of contact line during the necking; and R_a reduces continuously as increasing V and experiences a slight increase during the necking. Furthermore, for the two large R_{SHS} cases and during the beginning of bubble formation period $V/l_\sigma^3 < 3$ (i.e., before the contact line reaching to the edge of the SHS), the profiles showing as a function V for different R_{SHS} overlap, indicating that the bubble shape is only a function of V and independent of R_{SHS}.

Although the profiles of H, R_b, and R_a for different R_{SHS} share similar trends, there are notable differences. Comparing the results at a same V, as increasing R_{SHS}, the bubble has a smaller H, a larger R_b, and a larger R_a (i.e., the bubble is wider in the horizonal direction). For the two small $R_{SHS} = 4.2$ and 6.3 mm cases, R_b quickly increases to a maximum value of $R_b^{\max} = R_{SHS}$. However, for the largest $R_{SHS} = 19.0$ mm case, R_b very slowly reaches the maximum value of $R_b^{\max} = 7.5$ mm, which is smaller than R_{SHS}. As explained early, the two different trends correspond to two different bubble formation modes. For small R_{SHS} and mode A, the bubble base reaches and pins at the rim of SHS, so that $R_b^{\max} = R_{SHS}$. However, for large R_{SHS} and mode B, the bubble base is not able to reach to the edge of the SHS and the contact line continuously moves. The value of $R_b^{\max}$ in mode B depends on the equilibrium contact angle (θ_0) of the surface.[23,59]

C. Contact angle

Figure 6(a) shows the evolutions of contact angle (θ) as a function of time for three different R_{SHS}. Before the formation of bubble ($t \sim 0$), for all three cases, θ is close to 180° since the interface is nearly flat. However, with increasing time, the trends of θ are different among the three cases. For the small $R_{SHS} = 4.2$ and 6.3 mm (i.e., mode A), the evolutions of θ can be generally separated into three stages: At stage I ($0 < t < 0.65T_0$), with increasing time, θ reduces, indicating the deformation of three-phase contact line as bubble grows. This reduction is more obvious for smaller R_{SHS}. At stage II ($0.65 < t < 0.9T_0$), interestingly, θ maintains as a nearly constant value (denoted as $\theta_{\min}$), which suggests that the contact line does not deform further while the bubble continuously growing. The value of $\theta_{\min}$ is smaller for smaller R_{SHS}. For sufficiently small $R_{SHS} < 3$ mm, Qiao *et al.*[24] showed that $\theta_{\min}$ can be less than 90°. Finally, at stage III just before necking ($t > 0.9T_0$), θ experiences an either significant or mild increase, depending on the value of R_{SHS}. During the necking period ($t > 0.999T_0$) [Fig. 6(b)], θ has a nearly constant value of $\theta = \theta_0$, regardless of R_{SHS}. This result indicates that during the necking period and as the contact line retracts, the contact angle mainly depends on the material properties of the substrate.

For the largest $R_{SHS} = 19.0$ mm (mode B), with increasing time, θ continuously reduces until reaching a value close to θ_0 during the necking period. A period of constant value as bubble grows (the stage II in mode A) is not observed in mode B. The trend for

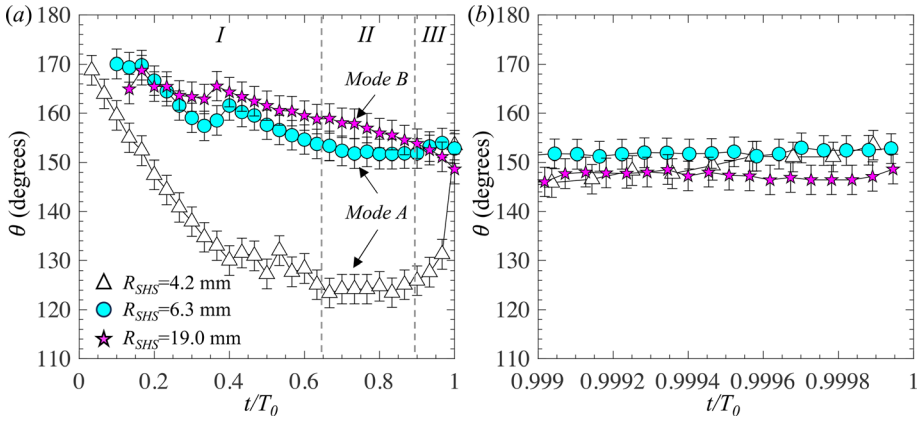

FIG. 6. (a) and (b) Variations of θ as a function of time for three SHSs. (b) The necking period.

$R_{SHS} = 19.0$ mm observed in the current study is in good agreement with Qiao *et al.*[24] However, Rubio-Rubio *et al.*[23] suggested a different trend that for mode B, and the contact angle remains nearly a constant of about 180° when the contact line moves. These different trends might be caused by various surface textures and θ_0 involved in different experiments. The SHS used by Rubio-Rubio *et al.* had a larger $\theta_0 = 166°$ than the one used in the current study ($\theta_0 = 152°$) and in Qiao *et al.* ($\theta_0 = 156°$).

While Qiao *et al.*[24] reported similar trends for θ, this study provides a more detailed discussion of θ at the necking period. We observed for the first time that θ has a nearly constant value of $\theta = \theta_0$, during the necking process, regardless of R_{SHS}. We also discussed the different trends of θ in the two different bubbling modes A and B.

D. Bubble necking

To better understand the pinch-off the gas bubble from the SHS, we discuss the evolutions of minimal neck radius. Figure 7(a) shows the time evolution of bubble shape just before the detachment for $R_{SHS} = 6.3$ mm. Bubble shapes for the other two cases, $R_{SHS} = 4.2$ and 19.0 mm, follow similar trends and are not shown. The time to pinch-off is defined as $\tau = T_0 - t$. The evolution of bubble shape shown in Fig. 7(a) is generally consistent with the results discussed in Secs. III B–III C: During the necking, H increases rapidly, R_b reduces, and θ remains nearly a constant. A neck seems to occur at $\tau \sim 20$ ms.

Figure 7(b) shows the evolutions of minimal neck radius [R_{neck}, defined in Fig. 7(a)] as a function of τ for three R_{SHS}. For all three cases

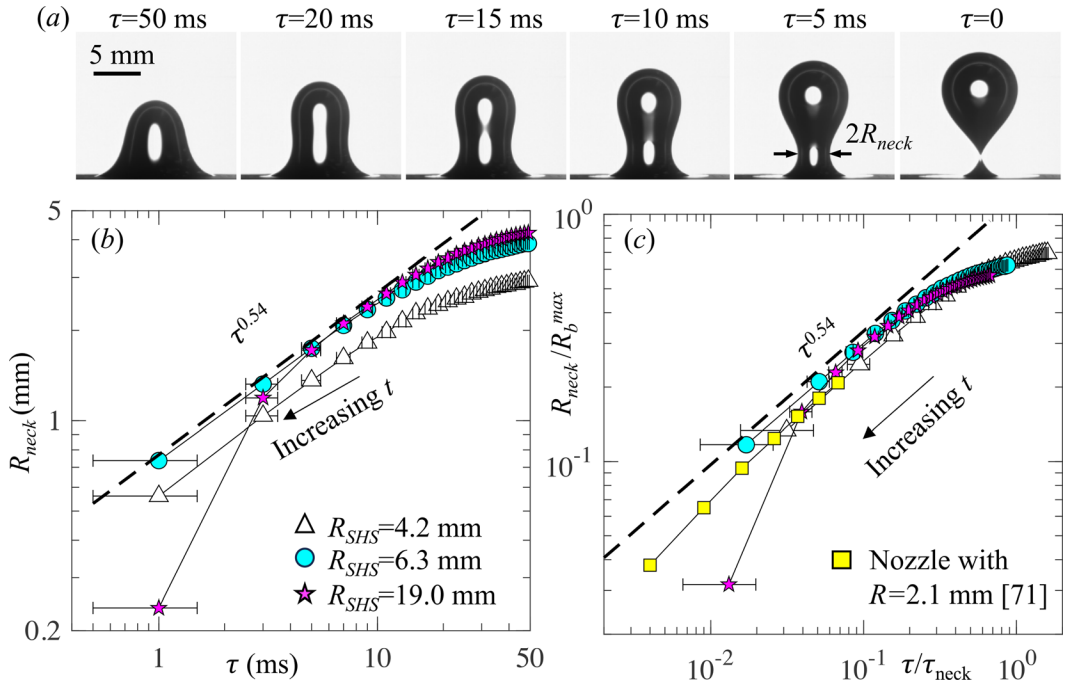

FIG. 7. (a) Evolutions of bubble shape during the necking period for $R_{SHS} = 6.4$ mm; and (b) and (c) variations of bubble neck radius in real units (b) and in normalized units (c). The error bars in (b) and (c) correspond to the uncertainty of time due to the data acquisition rate of 1000 frames per second.

(except for the largest R_{SHS} at $\tau < 3$ ms), R_{neck} reduces as increasing time and follows a power-law relation $R_{neck} \sim \tau^{0.54}$. The power-law exponent is in good agreement with these reported in the literature[69–72] for the pinch-off of a gas bubble from a nozzle submerged in water. This agreement indicates that the pinch-off of a gas bubble from SHS is similar to that from a nozzle, which can be predicted by the Rayleigh–Plesset equation, ignoring the effects of gas and liquid momentums.[69]

However, for the largest R_{SHS} at $\tau < 3$ ms, with increasing time, R_{neck} reduces at a rate faster than the prediction by the power-law relations. This deviation might be attributed to the reduction of R_b [as shown in Fig. 5(b)], which is different from the constant R_b during the necking for a bubble at a nozzle.[71] Since the reduction of R_b is most significantly for the largest R_{SHS} [Fig. 5(b)], the deviation is only seen for this case. Another possible reason for this deviation might be the uncertainty of time. The time of $\tau = 0$ is defined as the time (or frame) when the bubble just detached from the surface. Due to the finite 1000 frames-per-second data requisition rate in this work, the uncertainty of τ is 1 ms. To examine whether a similar deviation exists for the other two cases at $\tau < 1$ ms or whether the deviation is due to measurement error, a higher frame rate (e.g., 100 000 frames rate per second) is required. We leave this to future study.

In Fig. 7(c), the minimal neck radius is normalized by R_b^{max}, and the time is normalized by capillary-inertial timescale defined as $\tau_{neck} = (\rho_L {R_b}^{max3}/\sigma)^{0.5}$. The results obtained by Thoroddsen *et al.*[71] for the pinch-off of a bubble from a nozzle with radius $R = 2.1$ mm are also shown for comparison. Clearly, the results for different R_{SHS} are better collapsed compared to these before normalization. Moreover, the profiles for SHS largely overlap with the one for nozzle, except for the largest R_{SHS} at $\tau < 3$ ms. The overlapping of profiles on SHS and nozzle, again, indicates that the bubble pinch-off is universal. The time duration of pinch-off is governed by R_b^{max} and increases as increasing R_b^{max}.

E. Forces acting on the bubble

In this section, we discuss the six forces acting on the bubble, as defined in Table II. The magnitudes of six forces are calculated based on the bubble geomatical parameters and the expressions listed in Table II. Our goal is to understand how different forces are in balance and contribute to the quasi-static growth of the bubble. We show the results only for the bubble growing period, since in the necking period, the bubble is not in equilibrium. We find that the magnitudes of F_{GM}, F_{LI}, and F_D are nearly zero (supplementary material, Fig. S2), which is expected due to the small gas flow rate in the current study. The momentums of gas and liquid are negligible. Thus, the main forces acting on the bubble are F_P, F_B, and F_S, which are shown in Figs. 8(a)–8(c), respectively. Figure 8(d) shows the summation of the three forces.

First, we discuss the similarities among the three different R_{SHS}. For all cases, with increasing V, the magnitude of F_P increases primarily due to a smaller R_a and the raised gas pressure within the bubble. The magnitude of F_B also increases because of the larger H and the higher hydrostatic pressure acting on the bubble. The trend of F_S depends on R_{SHS}: For small R_{SHS} in mode A, the magnitude of F_S initially increases and then reaches a stable value, while for large R_{SHS} in mode B, the magnitude of F_S increases continuously. The variation of F_S is consistent with the change of contact angle as shown in Fig. 6. As shown in Fig. 8(d), the summation of these three forces, $F_P + F_B + F_S$, is close to zero. This result confirms that the bubble is governed by the balance among one lifting forces (pressure force) and two retaining forces (buoyancy force and surface tension force). This observation agrees with Rubio-Rubio *et al.*[23] who showed that the bubble shape can be predicted by the Young–Laplace equation, which is derived based on balance between surface tension and hydrostatic pressure. However, the balance of forces observed on SHS is very different from that at a nozzle, where the main lifting and retaining forces are F_B and F_S, respectively.[47]

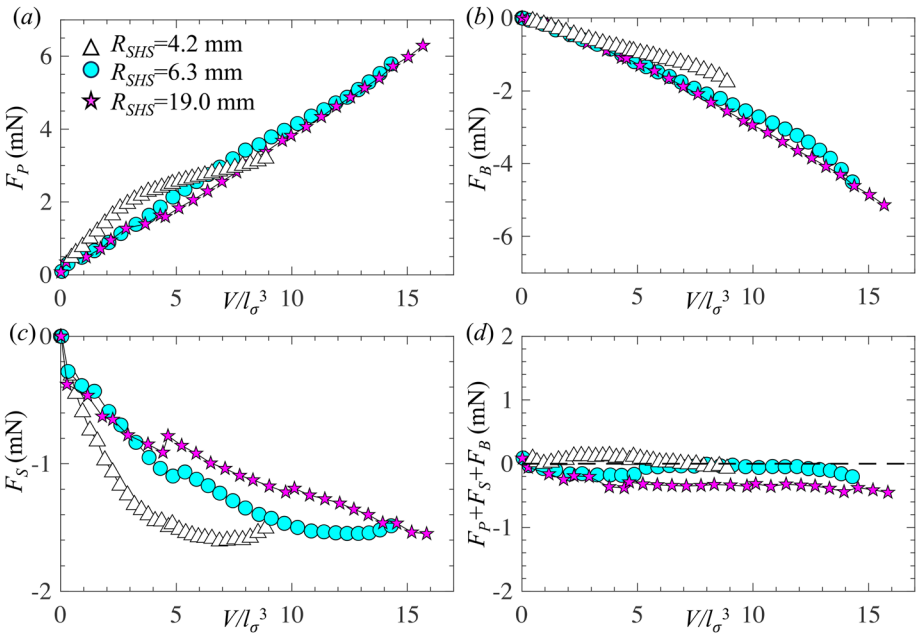

FIG. 8. (a)–(c) Variations of three main forces, pressure force (a), buoyancy force (b), surface tension force (c) acting on the bubble as a function of bubble volume, and (d) summation of the three forces. Other three forces (gas momentum force, liquid inertia force, and drag force) are close to 0 and are shown in supplementary material, Fig. S2.

Despite the similarities described above, there are notable differences among the three different R_{SHS}. As increasing R_{SHS}, the maximum value of $|F_P|$ increases from ~3 to ~6 mN, the maximum value of $|F_B|$ increases from ~2 to ~5 mN. The reason for these trends is because the maximum values of $|F_P|$ and $|F_B|$ are proportional to R_b^{max}, which increases as R_{SHS} increases. However, even though the maximum value of $|F_S|$ is also proportional to R_b^{max}, it does not increase with increasing R_{SHS}. Instead, it remains as a nearly constant of 1.6 mN. The trend is induced by the combination effects of larger R_b^{max} and larger contact angle with increasing R_{SHS}.

Typically, for a bubble growing from a nozzle, a detachment occurs when the buoyancy force overcomes the surface tension force. However, this is not the case here: the main lifting force (F_P) does not exceed the retaining forces during the bubble growing process. In fact, as explained by Rubio-Rubio *et al.*,[23] for bubble growing on a SHS, there is a maximum volume at which the bubble can maintain a stable shape. A detachment must occur when the bubble volume exceeds this maximum stable volume. We suspect that the necking process and the detachment are driven by the surface tension, which minimizes the surface area of the bubble. Due to the surface tension, the bubble quickly shrinks in the horizontal direction and changes into a spherical shape. Future studies are required to understand the force balance during the necking process.

F. Bubble detached volume

In this section, we compare the bubble detached volume (V_d) measured from the experiments to the theoretical prediction by Tate volume $V_T = 2\pi R_b^{max}\sigma/\rho_l g$.[45] Here, the Tate volume is derived based on the balance between surface tension force and buoyancy force, and the assumptions that the detached bubble is nearly spherical so that $F_B = \rho_l g V_T$ and has a contact angle of 90° so that the $F_S = 2\pi R_b^{max}\sigma$. At the quasi-static region, the Tate volume has been shown to well predict V_d for a bubble detaching from a nozzle[40,44] and from an orifice on hydrophilic and hydrophobic surfaces ($\theta_0 < 120°$).[61,62] However, it is unclear whether the Tate volume applies for a bubble detaching from the superhydrophobic surface ($\theta_0 > 150°$). To test this, Figs. 9(a) and 9(b) show V_d and V_d/V_T, respectively, as a function of R_b^{max}. The experimental data obtained by Rubio-Rubio *et al.*[23] and Qiao *et al.*[24] for SHS with $\theta_0 > 150°$ and by Mirsandi *et al.*[62] for hydrophilic and hydrophobic surfaces ($\theta_0 < 120°$) are also plotted. Clearly, regardless the types of surfaces and the values of θ_0, the Tate volume provides a good approximation for the bubble detached volume. Although the assumptions of spherical bubble shape and 90° contact angle used for deriving the Tate volume are not validated for SHS, the applicability of Tate volume is not affected.

The results shown in Figs. 9(a) and 9(b) indicate that regardless of the surface type, the bubble detached volume is linearly proportional to R_b^{max}. Surfaces with different wetting properties produce different R_b^{max}. Previous study[59] showed that for the hydrophilic surface, bubble formation followed mode A, and R_b^{max} was equal to the diameter of the orifice. For hydrophobic surface, bubble formation followed mode B, and R_b^{max} increased as θ_0 increases. Figure 9(c) shows R_b^{max} as a function of R_{SHS} for two different types of SHS (one from this work and

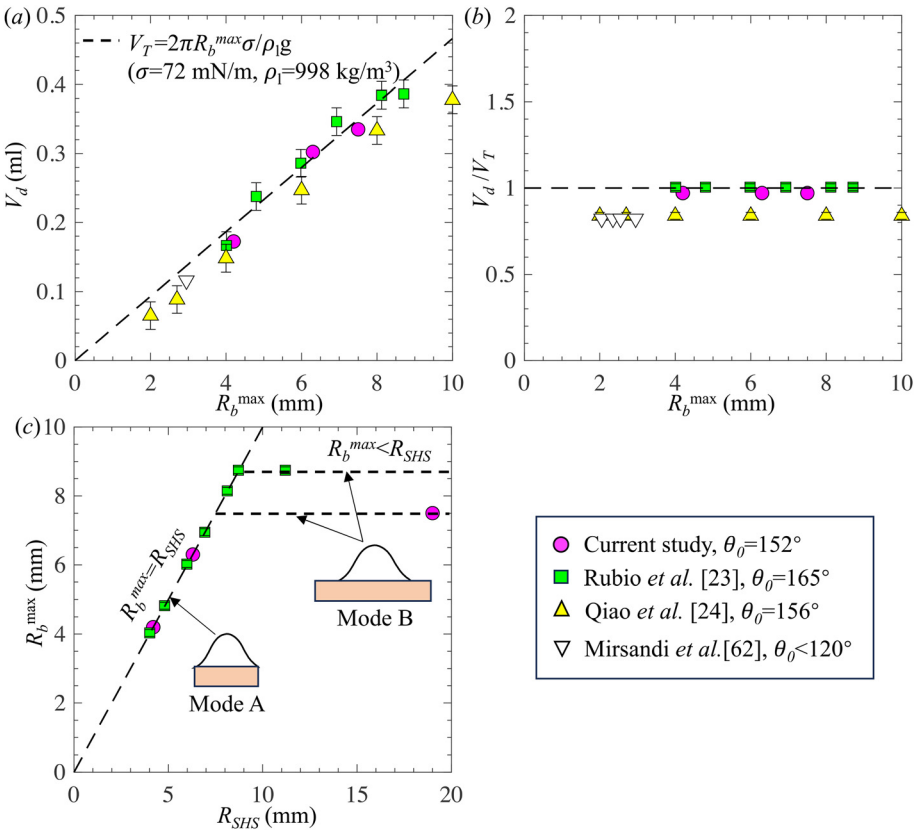

FIG. 9. (a) and (b) Bubble detached volume as a function of maximum bubble base radius: (a) detached volume shown in real unit, (b) detached volume normalized by Tate volume, and (c) maximum bubble base radius as a function of radius of the SHS.

one from Rubio-Rubio *et al.*[23]). Clearly, for SHS with small R_{SHS} where bubble formation follows mode A, $R_b^{max} = R_{SHS}$. However, for SHS with large R_{SHS} where bubble formation follows mode B, R_b^{max} is independent of R_{SHS} and might increase as θ_0 increases. Future studies are required to determine the relationship between R_b^{max} depends on θ_0. A bubble with smaller detached volume can be expected for SHS with smaller R_{SHS} and smaller θ_0.

IV. CONCLUSIONS

In summary, we experimentally measured bubble formation on three SHS with a radius R_{SHS} ranging from 4.2 to 19.0 mm. We studied the evolutions of bubble volume, bubble height, bubble base radius, bubble radius at the apex, contact angle, as well as the minimal neck radius. We also calculated six forces acting on the bubble during the growing process. The main conclusions are listed as follows:

- We observed two bubbling modes A and B, depending on R_{SHS}. In mode A for small R_{SHS}, the contact line quickly pins at the rim of SHS after an initial expansion. In mode B for large R_{SHS}, the contact line continuously expands as the bubble grows.
- For large R_{SHS}, we found a waiting time for a finite volume to be detected. The possible reason is that at the beginning of bubble formation, the radius at the apex is large, causing a nearly zero pressure force (which is the primary lifting force acting on the bubble).
- The contact angle follows different trends in the two bubbling modes: in mode A, θ initially reduced, then maintained as a constant, and finally increased; in mode B, θ continuously reduced. In both modes and during the necking, the contact line retracts, and θ is close to the equilibrium contact angle.
- For all R_{SHS}, the pinch-off of bubble on SHS at the early stage ($\tau > 1$ ms) follows a power-law relation $R_{neck} \sim \tau^{0.54}$, which agrees well with the pinch-off of bubble on a nozzle.
- At quasi-static region, the main forces acting on the bubble are one lifting force (pressure force) and two retaining forces (surface tension force and buoyancy force). As R_{SHS} increases, the maximum pressure force and maximum buoyancy force increase, while the maximum surface tension force remains nearly constant.
- Similar to hydrophilic and hydrophobic surfaces, Tate volume can be used to predict the detached bubble volume on SHS, which is a function of the maximum bubble base radius. A bubble with a smaller detached volume can be expected for SHS with smaller R_{SHS} and smaller θ_0.

Future studies will investigate the effects of flow rate, surface tension, contact angle, contact angle hysteresis, and texture geometries on the bubble formation on SHS and the detached bubble volume. A higher frame rate will be applied to investigate the impact of moving contact on the pinch-off of bubble on SHS.

SUPPLEMENTARY MATERIAL

See the supplementary material for supplementary Figs. S1 to S2.

ACKNOWLEDGMENTS

We thank the support of National Science Foundation under Grant Nos. 2041479 and 2339606, UMass Dartmouth's Marine and Undersea Technology (MUST) Research Program funded by the Office of Naval Research (ONR) under Grant No. N00014-20-1-2170, and University of Massachusetts OTCV Technology Development Fund. We also thank Paul Sousa for the assistance of fabricating the experimental setup.

AUTHOR DECLARATIONS

Conflict of Interest

The authors have no conflicts to disclose.

Author Contributions

Daniel O'Coin: Data curation (lead); Formal analysis (equal); Investigation (lead); Methodology (equal); Writing – original draft (equal). **Hangjian Ling:** Conceptualization (lead); Formal analysis (lead); Funding acquisition (lead); Resources (lead); Supervision (lead); Writing – original draft (equal); Writing – review & editing (lead).

DATA AVAILABILITY

The data that support the findings of this study are available from the corresponding author upon reasonable request.

REFERENCES

[1]X. Wang, J. Xu, H. Jiang, Y. Liu, X. Li, D. Shan, and B. Guo, "Achieving robust and enhanced pool boiling heat transfer using micro–nano multiscale structures," Appl. Therm. Eng. **227**, 120441 (2023).
[2]S. Y. Guan, Z. H. Zhang, R. Wu, X. K. Gu, and C. Y. Zhao, "Pool boiling inside micro-nano composite pores: Thermofluids behaviors and heat transfer enhancement," Appl. Phys. Lett. **124**, 093508 (2024).
[3]M. Hong, D. Mo, and Y. Heng, "Bubble dynamics analysis of pool boiling heat transfer with honeycomb micro-nano porous structured surfaces," Int. Commun. Heat Mass Transfer **152**, 107256 (2024).
[4]N. Xu, Z. Liu, X. Yu, J. Gao, and H. Chu, "Processes, models and the influencing factors for enhanced boiling heat transfer in porous structures," Renewable Sustainable Energy Rev. **192**, 114244 (2024).
[5]P. Pontes, R. Cautela, E. Teodori, A. Moita, Y. Liu, A. L. N. Moreira, A. Nikulin, and E. P. del Barrio, "Effect of pattern geometry on bubble dynamics and heat transfer on biphilic surfaces," Exp. Therm. Fluid Sci. **115**, 110088 (2020).
[6]S. Han, K. You, K. Kim, and J. Park, "Measurement of the attachment force between an air bubble and a mineral surface: Relationship between the attachment force and flotation kinetics," Langmuir **35**, 9364–9373 (2019).
[7]C. Corbett, Q. Wang, W. Smith, W. Liu, and A. D. Walmsley, "Cleaning effects due to shape oscillation of bubbles over a rigid boundary," Phys. Fluids **35**, 123335 (2023).
[8]N. Vyas, Q. X. Wang, K. A. Manmi, R. L. Sammons, S. A. Kuehne, and A. D. Walmsley, "How does ultrasonic cavitation remove dental bacterial biofilm?," Ultrason. Sonochem. **67**, 105112 (2020).
[9]G. Shakya, M. Cattaneo, G. Guerriero, A. Prasanna, S. Fiorini, and O. Supponen, "Ultrasound-responsive microbubbles and nanodroplets: A pathway to targeted drug delivery," Adv. Drug Delivery Rev. **206**, 115178 (2024).
[10]S. I. Kaykanat and A. K. Uguz, "The role of acoustofluidics and microbubble dynamics for therapeutic applications and drug delivery," Biomicrofluidics **17**, 021502 (2023).
[11]S. Roovers, T. Segers, G. Lajoinie, J. Deprez, M. Versluis, S. C. De Smedt, and I. Lentacker, "The role of ultrasound-driven microbubble dynamics in drug delivery: From microbubble fundamentals to clinical translation," Langmuir **35**, 10173–10191 (2019).
[12]S. Mohammadshahi, D. O'Coin, and H. Ling, "Impact of sandpaper grit size on drag reduction and plastron stability of super-hydrophobic surface in turbulent flows," Phys. Fluids **36**, 025139 (2024).
[13]H. Ling, S. Srinivasan, K. Golovin, G. H. McKinley, A. Tuteja, and J. Katz, "High-resolution velocity measurement in the inner part of turbulent boundary layers over super-hydrophobic surfaces," J. Fluid Mech. **801**, 670–703 (2016).

[14]H. Park, C.-H. Choi, and C.-J. Kim, "Superhydrophobic drag reduction in turbulent flows: A critical review," Exp. Fluids **62**, 229 (2021).
[15]W. Huang, J. Huang, Z. Guo, and W. Liu, "Icephobic/anti-icing properties of superhydrophobic surfaces," Adv. Colloid Interface Sci. **304**, 102658 (2022).
[16]S. S. Latthe, R. S. Sutar, A. K. Bhosale, S. Nagappan, C.-S. Ha, K. K. Sadasivuni, S. Liu, and R. Xing, "Recent developments in air-trapped superhydrophobic and liquid-infused slippery surfaces for anti-icing application," Prog. Org. Coat. **137**, 105373 (2019).
[17]X. Chang, M. Li, S. Tang, L. Shi, X. Chen, S. Niu, X. Zhu, D. Wang, and S. Sun, "Superhydrophobic micro-nano structured PTFE/WO_3 coating on low-temperature steel with outstanding anti-pollution, anti-icing, and anti-fouling performance," Surf Coat. Technol. **434**, 128214 (2022).
[18]M. Elius, S. Richard, K. Boyle, W. S. Chang, P. H. Moisander, and H. Ling, "Impact of gas bubbles on bacterial adhesion on super-hydrophobic aluminum surfaces," Res. Surf. Interfaces **15**, 100211 (2024).
[19]A. M. A. Mohamed, A. M. Abdullah, and N. A. Younan, "Corrosion behavior of superhydrophobic surfaces: A review," Arabian J. Chem. **8**, 749–765 (2015).
[20]T. Xiang, Y. Han, Z. Guo, R. Wang, S. Zheng, S. Li, C. Li, and X. Dai, "Fabrication of inherent anticorrosion superhydrophobic surfaces on metals," ACS Sustainable Chem. Eng. **6**, 5598–5606 (2018).
[21]A. Nosrati, S. Mohammadshahi, M. Raessi, and H. Ling, "Impact of the under-saturation level on the longevity of superhydrophobic surfaces in stationary liquids," Langmuir **39**, 18124–18131 (2023).
[22]A. B. D. Cassie and S. Baxter, "Wettability of porous surfaces," Trans. Faraday Soc. **40**, 546–551 (1944).
[23]M. Rubio-Rubio, R. Bolaños-Jiménez, C. Martínez-Bazán, J. C. Muñoz-Hervás, and A. Sevilla, "Superhydrophobic substrates allow the generation of giant quasi-static bubbles," J. Fluid Mech. **912**, A25 (2021).
[24]S. Qiao, C. Cai, W. Chen, C. Pan, and Y. Liu, "Control of the shape of bubble growth on underwater substrates with different sizes of superhydrophobic circles," Phys. Fluids **34**, 067110 (2022).
[25]S. H. Huynh, A. A. A. Zahidi, M. Muradoglu, B. H.-P. Cheong, and T. W. Ng, "Plastron-mediated growth of captive bubbles on superhydrophobic surfaces," Langmuir **31**, 6695–6703 (2015).
[26]J. Breveleri, S. Mohammadshahi, T. Dunigan, and H. Ling, "Plastron restoration for underwater superhydrophobic surface by porous material and gas injection," Colloids Surf., A **676**, 132319 (2023).
[27]A. A. Kulkarni and J. B. Joshi, "Bubble formation and bubble rise velocity in gas−liquid systems: A review," Ind. Eng. Chem. Res. **44**, 5873–5931 (2005).
[28]R. Kumar and N. K. Kuloor, "The formation of bubbles and drops," in *Advances in Chemical Engineering*, edited by T. B. Drew, G. R. Cokelet, J. W. Hoopes, and T Vermeulen (Academic Press, 1970), pp. 255–368.
[29]S. L. Anna, "Droplets and bubbles in microfluidic devices," Annu. Rev. Fluid Mech. **48**, 285–309 (2016).
[30]J. Rodríguez-Rodríguez, A. Sevilla, C. Martínez-Bazán, and J. M. Gordillo, "Generation of microbubbles with applications to industry and medicine," Annu. Rev. Fluid Mech. **47**, 405–429 (2015).
[31]A. Georgoulas, P. Koukouvinis, M. Gavaises, and M. Marengo, "Numerical investigation of quasi-static bubble growth and detachment from submerged orifices in isothermal liquid pools: The effect of varying fluid properties and gravity levels," Int. J. Multiphase Flow **74**, 59–78 (2015).
[32]K. Terasaka and H. Tsuge, "Bubble formation at a single orifice in non-Newtonian liquids," Chem. Eng. Sci. **46**, 85–93 (1991).
[33]Y. Zhou, B. Ji, C. Zhao, and H. Bo, "Bubble formation from a submerged orifice in a thin liquid layer: Detachment and bursting," Phys. Fluids **33**, 013305 (2021).
[34]S. Vafaei and D. Wen, "Effect of gold nanoparticles on the dynamics of gas bubbles," Langmuir **26**, 6902–6907 (2010).
[35]S. Vafaei and D. Wen, "Spreading of triple line and dynamics of bubble growth inside nanoparticle dispersions on top of a substrate plate," J. Colloid Interface Sci. **362**, 285–291 (2011).
[36]B. Ji, Z. Yang, and J. Feng, "Oil-coated bubble formation from submerged coaxial orifices," Phys. Rev. Fluids **6**, 33602 (2021).
[37]O. Pamperin and H.-J. Rath, "Influence of buoyancy on bubble formation at submerged orifices," Chem. Eng. Sci. **50**, 3009–3024 (1995).
[38]I. Chakraborty, B. Ray, G. Biswas, F. Durst, A. Sharma, and P. S. Ghoshdastidar, "Computational investigation on bubble detachment from submerged orifice in quiescent liquid under normal and reduced gravity," Phys. Fluids **21**, 062103 (2009).
[39]E. Mohseni, M. E. Chiamulera, S. F. Reinecke, and U. Hampel, "Bubble formation from sub-millimeter orifices: Experimental analysis and modeling," Chem. Eng. Process. **173**, 108809 (2022).
[40]Y. Zhou, B. Ji, X. Yan, P. Jin, J. Li, and N. Miljkovic, "Asymmetric bubble formation at rectangular orifices," Langmuir **37**, 4302–4307 (2021).
[41]P. Hanafizadeh, A. Sattari, S. E. Hosseini-Doost, A. G. Nouri, and M. Ashjaee, "Effect of orifice shape on bubble formation mechanism," Meccanica **53**, 2461–2483 (2018).
[42]S. Vafaei, T. Borca-Tasciuc, and D. Wen, "Theoretical and experimental investigation of quasi-steady-state bubble growth on top of submerged stainless steel nozzles," Colloids Surf., A **369**, 11–19 (2010).
[43]J. Ma, J. Li, P. Zhou, Y. Song, L. Chai, and C. Q. Zhou, "A viewpoint on the dynamics of bubble formation from a submerged nozzle," Eur. J. Mech. B **78**, 276–283 (2019).
[44]S. D. Bari and A. J. Robinson, "Experimental study of gas injected bubble growth from submerged orifices," Exp. Therm. Fluid Sci. **44**, 124–137 (2013).
[45]T. Tate, "On the magnitude of a drop of liquid formed under different circumstances," London, Edinburgh Dublin Philos. Mag. J. Sci. **27**, 176–180 (1864).
[46]S. Vafaei, P. Angeli, and D. Wen, "Bubble growth rate from stainless steel substrate and needle nozzles," Colloids Surf., A **384**, 240–247 (2011).
[47]S. Vafaei and D. Wen, "Bubble formation on a submerged micronozzle," J. Colloid Interface Sci. **343**, 291–297 (2010).
[48]M. S. Longuet-Higgins, B. R. Kerman, and K. Lunde, "The release of air bubbles from an underwater nozzle," J. Fluid Mech. **230**, 365–390 (1991).
[49]H. N. Oguz and A. Prosperetti, "Dynamics of bubble growth and detachment from a needle," J. Fluid Mech. **257**, 111–145 (1993).
[50]M. Jamialahmadi, M. R. Zehtaban, H. Müller-Steinhagen, A. Sarrafi, and J. M. Smith, "Study of bubble formation under constant flow conditions," Chem. Eng. Res. Des. **79**, 523–532 (2001).
[51]J. A. Simmons, J. E. Sprittles, and Y. D. Shikhmurzaev, "The formation of a bubble from a submerged orifice," Eur. J. Mech. B **53**, 24–36 (2015).
[52]H. Wong, D. Rumschitzki, and C. Maldarelli, "Theory and experiment on the low-Reynolds-number expansion and contraction of a bubble pinned at a submerged tube tip," J. Fluid Mech. **356**, 93–124 (1998).
[53]V. K. Badam, V. Buwa, and F. Durst, "Experimental investigations of regimes of bubble formation on submerged orifices under constant flow condition," Can. J. Chem. Eng. **85**, 257–267 (2007).
[54]C. Qu, Y. Yu, and J. Zhang, "Experimental study of bubbling regimes on submerged micro-orifices," Int. J. Heat Mass Transfer **111**, 17–28 (2017).
[55]Y. Chen, S. Liu, R. Kulenovic, and R. Mertz, "Experimental study on macroscopic contact line behaviors during bubble formation on submerged orifice and comparison with numerical simulations," Phys. Fluids **25**, 092105 (2013).
[56]S. V. Gnyloskurenko, A. V. Byakova, O. I. Raychenko, and T. Nakamura, "Influence of wetting conditions on bubble formation at orifice in an inviscid liquid. Transformation of bubble shape and size," Colloids Surf., A **218**, 73–87 (2003).
[57]S. Gnyloskurenko, A. Byakova, T. Nakamura, and O. Raychenko, "Influence of wettability on bubble formation in liquid," J. Mater. Sci. **40**, 2437–2441 (2005).
[58]A. V. Byakova, S. V. Gnyloskurenko, T. Nakamura, and O. I. Raychenko, "Influence of wetting conditions on bubble formation at orifice in an inviscid liquid: Mechanism of bubble evolution," Colloids Surf., A **229**, 19–32 (2003).
[59]D. Gerlach, G. Biswas, F. Durst, and V. Kolobaric, "Quasi-static bubble formation on submerged orifices," Int. J. Heat Mass Transfer **48**, 425–438 (2005).
[60]Y. Nam, J. Wu, G. Warrier, and Y. S. Ju, "Experimental and numerical study of single bubble dynamics on a hydrophobic surface," J. Heat Transfer **131**, 121004 (2009).
[61]G. Corchero, A. Medina, and F. J. Higuera, "Effect of wetting conditions and flow rate on bubble formation at orifices submerged in water," Colloids Surf., A **290**, 41–49 (2006).
[62]H. Mirsandi, W. J. Smit, G. Kong, M. W. Baltussen, E. A. J. F. Peters, and J. A. M. Kuipers, "Influence of wetting conditions on bubble formation from a submerged orifice," Exp. Fluids **61**, 83 (2020).
[63]A. K. Chesters, "Modes of bubble growth in the slow-formation regime of nucleate pool boiling," Int. J. Multiphase Flow **4**, 279–302 (1978).

[64]S. Mohammadshahi, J. Breveleri, and H. Ling, "Fabrication and characterization of super-hydrophobic surfaces based on sandpapers and nano-particle coatings," Colloids Surf., A **666**, 131358 (2023).
[65]E. Mohseni, J. Jose Kalayathine, S. F. Reinecke, and U. Hampel, "Dynamics of bubble formation at micro-orifices under constant gas flow conditions," Int. J. Multiphase Flow **132**, 103407 (2020).
[66]K. Loubière and G. Hébrard, "Bubble formation from a flexible hole submerged in an inviscid liquid," Chem. Eng. Sci. **58**, 135–148 (2003).
[67]J. Xie, X. Zhu, Q. Liao, H. Wang, and Y.-D. Ding, "Dynamics of bubble formation and detachment from an immersed micro-orifice on a plate," Int J. Heat Mass Transfer **55**, 3205–3213 (2012).
[68]J. Zhang, Y. Yu, C. Qu, and Y. Zhang, "Experimental study and numerical simulation of periodic bubble formation at submerged micron-sized nozzles with constant gas flow rate," Chem. Eng. Sci. **168**, 1–10 (2017).
[69]J. C. Burton, R. Waldrep, and P. Taborek, "Scaling and instabilities in bubble pinch-off," Phys. Rev. Lett. **94**, 184502 (2005).
[70]N. C. Keim, P. Møller, W. W. Zhang, and S. R. Nagel, "Breakup of air bubbles in water: Memory and breakdown of cylindrical symmetry," Phys. Rev. Lett. **97**, 144503 (2006).
[71]S. T. Thoroddsen, T. G. Etoh, and K. Takehara, "Experiments on bubble pinch-off," Phys. Fluids **19**, 042101 (2007).
[72]S. Quan and J. Hua, "Numerical studies of bubble necking in viscous liquids," Phys. Rev. E **77**, 66303 (2008).